

Chapter 7

Palladium In An Oxygen And CO Gas Phase

As a next step towards a better understanding of the CO oxidation reaction on the Pd(100) surface, also the second reactant, the CO, has to be taken into account. Again the atomistic thermodynamics approach is used to obtain a first idea about the stability of the different structures under realistic gas phase conditions, i.e. temperatures and pressures as applied in heterogeneous catalysis ($p \approx 1$ atm, $T \approx 300 - 600$ K). Since in this work the atomistic thermodynamics approach is used to compare the stability of all considered structures, it is important to include as many potentially relevant structures as possible. Thus, at the beginning of this Chapter the considered surface structures are introduced and in the last Section their thermodynamic stability in a constrained equilibrium with an oxygen and CO gas phase is evaluated.

7.1 CO Adsorption On Pd(100)

As already discussed in Section 6.1 the Pd(100) surface exhibits three high symmetry adsorption sites, a bridge, a top and a fourfold hollow site. Experimentally, the adsorption of CO on Pd(100) has been studied intensively [127–134]. One of the first and most detailed studies is the work by Bradshaw and Hoffmann [127] combining infrared adsorption spectroscopy (IRAS) and low-energy electron diffraction (LEED). They find that at all coverages CO adsorbs upright in bridge position. At a coverage of $\Theta = 0.5$ ML an ordered $(2\sqrt{2} \times \sqrt{2})R45^\circ$ overlayer is formed, which is compressed to a $(3\sqrt{2} \times \sqrt{2})R45^\circ$ structure at $\Theta = 0.67$ ML and a $(4\sqrt{2} \times \sqrt{2})R45^\circ$ at $\Theta = 0.75$ ML. These results have been confirmed by further LEED [129–131, 134] and IRAS [132] studies as well as high resolution electron energy loss spectroscopy (HREELS) [129, 131] and surface core-level shift (SCLS) measurements [133].

The formation of the $(2\sqrt{2} \times \sqrt{2})R45^\circ$ rather than a simple $c(2 \times 2)$ structure has been attributed to the minimization of the strongly repulsive interactions between the adsorbed CO molecules. In the $c(2 \times 2)$ structure each molecule has four nearest

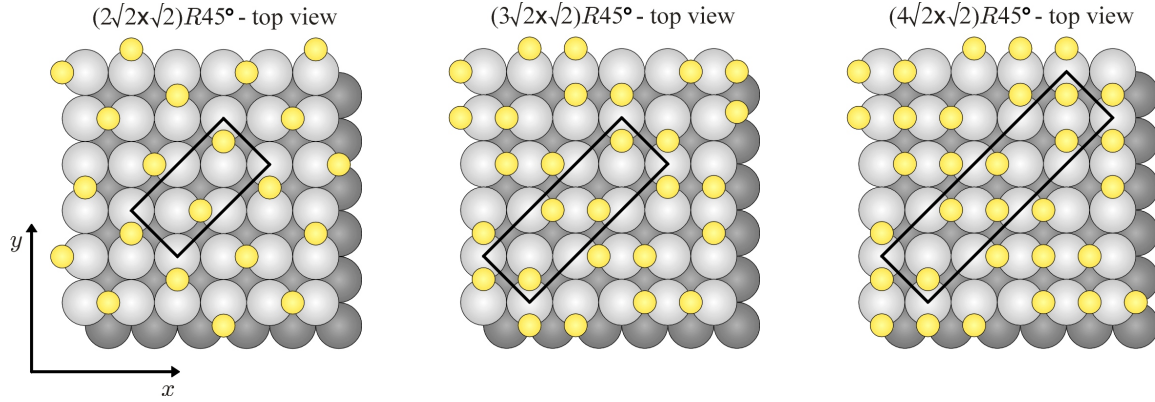


Figure 7.1: Schematic illustration of the three experimentally characterized adlayer structures of CO on Pd(100). From left to right the coverage increases from $\Theta = 0.5$ to $\Theta = 0.67$ and $\Theta = 0.75$ ML. The yellow small spheres represent the CO molecules, the grey large spheres the Pd(100) surface (second layer atoms are darkened).

neighbors at a distance of $\sqrt{2}a$, where a is the length of the (1×1) surface unit cell. In the $(2\sqrt{2} \times \sqrt{2})R45^\circ$ structure, however, the CO molecules form a distorted hexagonal overlayer with only two neighbors at a distance of $\sqrt{2}a$ and four neighbors slightly further away at $\sqrt{5/2}a$.

A schematic illustration of the three experimentally characterized adlayer structures is shown in Fig. (7.1). In addition to these structures also simple (1×1) and (2×2) overlayers with CO in bridge, top and hollow sites will be considered in this study. The binding energies of all considered structures are listed in Tab. 7.1 for the PBE, RPBE and LDA exchange-correlation functional. The muffin tin radius for the carbon is set to $R_{\text{MT}}^{\text{C}} = 1.0$ bohr and a $[10 \times 10 \times 1]$ MP grid is used for the (1×1) structures. For the three $(n\sqrt{2} \times \sqrt{2})R45^\circ$ structures $[4 \times 8 \times 1]$ (for $n = 2$) and $[2 \times 8 \times 1]$ (for $n = 3, 4$) MP-grids are used. All other computational parameters are equivalent to the ones given on Page 66. For a detailed discussion of the computational setup cf. Appendix A.2.

Looking at the binding energies it can be seen that the average binding energy per CO molecule is almost constant up to a coverage of $\Theta = 0.5$ ML. For higher coverages the binding energy decreases rapidly. It should be noted that in agreement with the experimental findings the bridge site is also the energetically most stable one at all coverages for the two GGA functionals. For the LDA functional, though, the hollow site seems to be preferred at low coverages. The failure in the prediction of the right adsorption site for CO in the low coverage limit on transition metal surfaces due to the approximate exchange-correlation functional is a known problem within DFT. The most prominent example for this is the adsorption of CO on the platinum (111) surface. Here, it is experimentally observed, that the CO occupies the low-coordination top site, whereas in DFT calculations for both the LDA and the PBE the high-coordinated hollow site is preferred [135]. Nevertheless, for the here

	Coverage	PBE	RPBE	LDA
$(2\sqrt{2} \times \sqrt{2})R45^\circ$	0.50	-1.92	-1.55	-2.74
$(3\sqrt{2} \times \sqrt{2})R45^\circ$	0.67	-1.73	-1.36	-2.55
$(4\sqrt{2} \times \sqrt{2})R45^\circ$	0.75	-1.63	-1.25	-2.45
$p(2 \times 2)\text{-CO}^{\text{br}}$	0.25	-1.92	-1.55	-2.73
$p(2 \times 2)\text{-CO}^{\text{hol}}$	0.25	-1.84	-1.40	-2.86
$p(2 \times 2)\text{-CO}^{\text{top}}$	0.25	-1.52	-1.21	-2.20
$c(2 \times 2)\text{-CO}^{\text{br}}$	0.50	-1.92	-1.54	-2.74
$c(2 \times 2)\text{-CO}^{\text{hol}}$	0.50	-1.71	-1.26	-2.72
$c(2 \times 2)\text{-CO}^{\text{top}}$	0.50	-1.50	-1.19	-2.17
$(1 \times 1)\text{-CO}^{\text{br}}$	1.00	-1.31	-0.90	-2.21
$(1 \times 1)\text{-CO}^{\text{hol}}$	1.00	-0.83	-0.39	-1.83
$(1 \times 1)\text{-CO}^{\text{top}}$	1.00	-0.96	-0.60	-1.75

Table 7.1: Average binding energies per CO molecule on Pd(100). All values are in eV.

discussed system, the GGA functionals do predict the correct adsorption site and for a coverage of $\Theta = 0.5$ ML also within the LDA the bridge site is again the most stable one. At $\Theta = 0.5$ ML, the experimentally proposed $(2\sqrt{2} \times \sqrt{2})R45^\circ$ structure shows only a negligible lower binding energy than the $c(2 \times 2)$ structure (few meV). Overall, DFT seems to work rather well for the prediction of the right adsorption site as well as of the lowest energy adlayer for this system, independent of the chosen exchange-correlation functional. The absolute values of the binding energies, though, show strong deviations for the different functionals, which is another known problem in DFT, the consequences of which will be discussed at the end of this Chapter. Comparing to previous DFT studies the obtained results are fully consistent [51, 136].

7.2 Co-Adsorption Of Oxygen And CO

Simple Adlayers

With the present understanding two different kinds of co-adsorption structures of O and CO can be identified in this particular system. They can either form some adlayer structure on the Pd(100) surface or they can involve the reconstructed $(\sqrt{5} \times \sqrt{5})R27^\circ$ surface oxide structure. Focusing first on the mixed adlayers of oxygen and CO on Pd(100) it should be noted that experimentally no ordered overlayer structures of O and CO have hitherto been observed. If the Pd(100) surface is exposed to both gas phase species, it has instead been found that the two adsorbates form separate domains [110]. In these low energy electron diffraction (LEED) experiments they observed that for a fully developed $p(2 \times 2)\text{-O}/\text{Pd}(100)$ surface the $p(2 \times 2)$ LEED pattern disappeared upon exposure to CO at $T = 80$ K. Assuming an approximate barrier of 1.0 eV for the reaction of O and CO on the Pd(100) surface to form CO_2 [137,

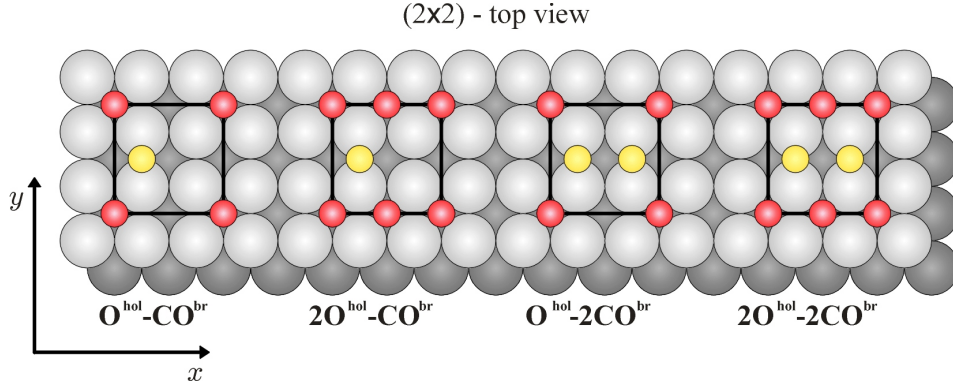


Figure 7.2: Schematic illustration of the co-adsorbed overlayer structures of oxygen and CO on Pd(100). The small red spheres correspond to oxygen atoms, the small yellow spheres represent the CO molecules and the large grey spheres the Pd(100) surface.

	Coverage	PBE	RPBE	LDA
(2×2) -O ^{hol} -CO ^{br}	0.50	-2.95	-2.26	-4.53
(2×2) -2O ^{hol} -CO ^{br}	0.75	-2.93	-1.91	-5.12
(2×2) -O ^{hol} -2CO ^{br}	0.75	-3.96	-2.85	-6.40
(2×2) -2O ^{hol} -2CO ^{br}	1.00	-3.64	-2.22	-6.69

Table 7.2: Total binding energies of O and CO on Pd(100) with respect to gas phase O₂ and CO. All values are in eV.

138] it is rather unlikely that the adsorbed oxygen was reacted with the CO at this low temperature. The vanishing of the LEED pattern was thus interpreted as a CO induced disordering of the oxygen islands. This behavior was explained by strongly repulsive, lateral interactions between the adsorbates. To nevertheless obtain an idea about the binding energies of O and CO in such mixed overlayer structures, different models that seem to be most obvious from a combinatorial point of view are set up. For this a (2×2) surface unit cell is used containing 1–2 O and CO adsorbates. Here, the adsorbates are only considered in their most favorite adsorption sites, i.e. the oxygen atoms sit in hollow sites and the CO atoms in bridge sites. Discarding structures, in which the adsorbates sit at distances smaller than the length of the (1×1) surface unit cell, this leads to the four different structures shown in Fig. 7.2. The corresponding total binding energies of all adsorbates, given by

$$E_{\text{O,CO@Pd(100)}}^{\text{bind}} = E_{\text{O,CO@Pd(100)}}^{\text{tot}} - E_{\text{Pd(100)}}^{\text{tot}} - N_{\text{O}}1/2E_{\text{O}_2}^{\text{tot}} - N_{\text{CO}}E_{\text{CO}}^{\text{tot}} \quad , \quad (7.1)$$

are listed in Tab. 7.2. The computational setup for obtaining these values is equivalent to the one described in the previous Section.

Similar to the pure adlayer structures of O and CO on Pd(100) also the mixed overlayers show a decrease in the binding energy per adsorbate with increasing coverage,

which reflects the afore mentioned repulsive interactions between the two species. A comparison of the thermodynamic stability of the co-adsorption structures in a constrained equilibrium with an O_2 and CO gas phase, will be discussed in the next Section. Comparing the values of the binding energies for the different exchange-correlation functionals they do not seem to agree very well. It is a known problem, though, that the LDA and GGA exchange-correlation functionals do not describe the O-O binding energy in the O_2 and the C-O binding energy in the CO molecule very well. The average deviation in the binding energies per O atom resp. per CO molecule on the surface between the different functionals appears to be rather constant. Considering, e.g., an average deviation of 1.0 eV per O and 1.3 eV per CO between the RPBE and LDA binding energies the obtained results are consistent. Similarly, for the difference between the RPBE and PBE binding energies an average deviation of 0.3 eV per O and 0.4 eV per CO can be observed. For a coverage of $\Theta = 0.5$ ML the binding energy of the co-adsorbed phase is ~ 30 – 70 meV smaller than the sum of the binding energies of the respective $c(2 \times 2)$ phases for each species. Thus, the repulsive interactions between O and CO are even stronger than the interactions between O and O, resp. CO and CO in the pure phases. The adsorption of both O and CO in hollow sites in a $c(2 \times 2)$ structure gives an even smaller binding energy.

Also on Pd(111) it has been observed that adsorbed O and CO aggregate into separate domains rather than building a mixed phase [139, 140]. It should be noted that the findings for the two Pd surfaces are in contrast to the findings for the Ru(0001), Rh(111), Ni(111) and Pt(111) surfaces. Here, several O and CO co-adsorbed structures have been identified (cf. Ref. [141] and references therein).

O And CO On The $(\sqrt{5} \times \sqrt{5})R27^\circ$ Surface Oxide

A second possibility to obtain co-adsorbed structures of oxygen and CO is the additional adsorption of CO on and/or partial substitution of oxygen by CO in the $(\sqrt{5} \times \sqrt{5})R27^\circ$ surface oxide structure. As can be seen in Fig. 7.3 the surface oxide structure exhibits top, bridge and hollow sites. Due to the symmetry of the underlying Pd(100) substrate multiple sites of one type are very similar, but not completely equivalent. Only the top sites differ substantially, depending if the corresponding palladium atom is twofold or fourfold coordinated by oxygen atoms. For the adsorption of CO on the $(\sqrt{5} \times \sqrt{5})R27^\circ$ structure there has been no experimental information available. Consequently, a systematic search starting with the adsorption sites depicted in Fig. 7.3 is performed. A schematic illustration of all considered structures is given in Appendix B.1. Adsorbing only one additional CO molecule on the surface oxide in any of the ten shown sites already shows that the four hollow sites are not stable at all. Upon relaxation, the CO molecule always moves to the corresponding bridge site. The binding energies of the 2 bridge sites are almost degenerated, as expected from the symmetry of the surface unit cell. The same is observed for the 2 twofold and the 2 fourfold by oxygen coordinated top sites, respectively. Thus, in the following such pairs of sites will be treated as equivalent from an energetic point of

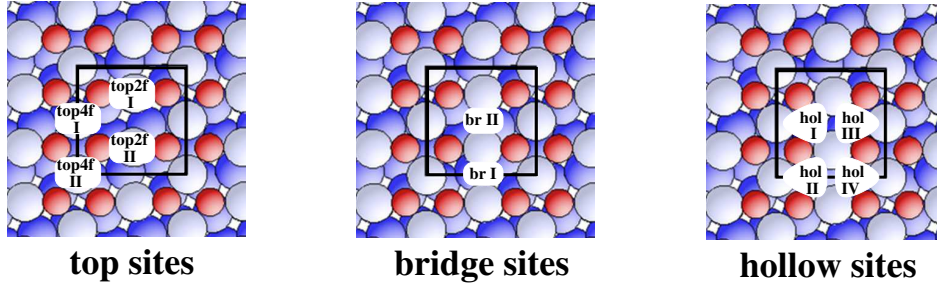


Figure 7.3: High-symmetry adsorption sites on the $(\sqrt{5} \times \sqrt{5})R27^\circ$ surface oxide structure. Red small spheres represent the lattice oxygen atoms, large light-blue ones the reconstructed Pd atoms and large dark-blue spheres Pd atoms belong to the underlying Pd(100) substrate.

Adsorption Structure	E^{bind}	Adsorption Structure	E^{bind}
CO^{br}	-0.93	2CO^{br}	-0.75
CO^{top2f}	-0.62	$2\text{CO}^{\text{top2f}}$	-0.51
CO^{top4f}	-0.13	—	—

Table 7.3: Average binding energies of CO on $(\sqrt{5} \times \sqrt{5})R27^\circ$ surface oxide structure calculated within PBE. All values are per CO molecule and in eV.

view. Similar to the CO adsorption on the clean Pd(100) surface, also here the bridge site is the most stable one. The binding energies with respect to the surface oxide structure, i.e.

$$E_{\text{CO}@(\sqrt{5} \times \sqrt{5})R27^\circ}^{\text{bind}} = E_{\text{CO}@(\sqrt{5} \times \sqrt{5})R27^\circ}^{\text{tot}} - E_{(\sqrt{5} \times \sqrt{5})R27^\circ}^{\text{tot}} - N_{\text{CO}} E_{\text{CO}}^{\text{tot}}, \quad (7.2)$$

where N_{CO} is the number of adsorbed CO molecules, are given in Tab. 7.3 for one and two CO molecules per surface unit cell (structures 1–3, 15–17 in Appendix B.1). A structure with two CO molecules adsorbed on both of the fourfold coordinated top sites ($2\text{CO}^{\text{top4f}}$, structure 17) is not stable upon relaxation. Mixing the adsorption sites (structures 18–20), i.e. placing e.g. one CO in a bridge site and a second one in a twofold top site does always yield less stable structures than the adsorption in like sites due to strongly repulsive interactions between the adsorbed molecules. Also for the same reason, any structure containing more than two additional CO molecules per surface unit cell results as unstable.

Instead of adsorbing two CO molecules it is also possible to simultaneously adsorb one CO and one O in the different sites (structures 81–89). This leads to stable structures, only if both O and CO are sitting in a bridge or a twofold coordinated top site or O in bridge and CO in a fourfold coordinated top site (structures 81,82,87). Again the adsorption in bridge sites gives the most stable structure.

Since there are noticeable nearest neighbor interactions between the adsorbates

within the $(\sqrt{5} \times \sqrt{5})R27^\circ$ surface unit cell, calculations in larger $(\sqrt{5} \times \sqrt{5})R27^\circ$ surface unit cells are performed to check, if there are also interactions between adsorbates in neighboring surface unit cells. For this oxygen and CO are adsorbed in bridge sites in (2×1) and (1×2) surface unit cells (a detailed description can be found in Appendix B.2). It could be shown, that the nearest neighbor interactions do not extend beyond the “ (1×1) ” surface unit cell.

To increase the configurational space of considered co-adsorption structures, configurations, in which the original surface oxide is modified, are also considered. In a first step, one of the upper, hollow site oxygen atoms (cf. Fig 6.3) is removed from the $(\sqrt{5} \times \sqrt{5})R27^\circ$ structure and CO and O are again adsorbed in the afore described sites (structures 8–11, 29–32 and 47–49). Here, Eq. (7.2) is not applicable anymore to directly compare the binding energies of the adsorbates with those on the unmodified surface oxide structure. Instead, the stability of all these structures will be compared within the atomistic thermodynamics approach in Section 7.3.

If both of the upper oxygen atoms are removed, the surface oxide structure is already somewhat destabilized. Since this leads to a rather open structure (only four reconstructed Pd atoms on five Pd(100) substrate atoms), the structural relaxation showed, that the palladium atoms can then move quite easily in lateral directions on the surface. Here, the additional adsorption of one or two CO molecules or one O and one CO leads only to stable structures, if just CO sits in bridge or twofold top sites (structures 37–39, 61–63 and 69–71).

A further considered modification of the $(\sqrt{5} \times \sqrt{5})R27^\circ$ structure is the substitution of one or both of the upper oxygen atoms by CO. Again it is then possible to adsorb additional CO on the other 4 top sites and 2 bridge sites (structures 4–7, 21–28, 40–46, 54–59, 64, 72–74, 78–80 and 90–92). If the CO substitutes the upper oxygen atoms, also the additional adsorption of a sole O atom in any of the sites does still give a mixed structure. This is only possible in bridge sites, though, whereas almost all structures with O adsorbed on top sites are not stable upon relaxation. Substituting only one of the upper O atoms in the surface oxide structure by CO and removing the second one leads to the same findings (structures 12–14, 33–36, 50–53, 60, 65–68 and 75–77).

Leaving out the four unstable hollow sites, from a pure combinatorial point of view there are 168 possible co-adsorption structures involving the reconstructed $(\sqrt{5} \times \sqrt{5})R27^\circ$ surface unit cell. Since there is only little known about the co-adsorption of O and CO on the $(\sqrt{5} \times \sqrt{5})R27^\circ$ surface oxide, none of the possible structures can easily be excluded. Nevertheless, considering e.g. the interactions between the adsorbates already quite a number of structures can be discarded without performing extensive DFT calculations. Since all structures with two adsorbates on mixed site types (i.e. br-top2f etc.) appear to be rather unstable, the number of reasonable structures is already reduced to 92 (cf. Appendix B.1). Out of these structures only 55 are stable upon relaxation. All other structures exhibit either too strongly repulsive interactions between the different adsorbates leading effectively to a desorption of the adsorbates, or the reconstructed palladium layer is so much distorted, that the

adsorbates can not be considered as being in their original adsorption sites anymore.

Confirming The Adsorption Site — SCLS Measurements

Only very recently surface core level shift (SCLS) measurements have been performed for the surface oxide structure having additional CO adsorbed [142]. Since the core-level position is sensitive to the local coordination of an atom, a comparison between the SCLS spectrum of the *clean* $(\sqrt{5} \times \sqrt{5})R27^\circ$ structure and the surface oxide structure + CO could provide information about the adsorption site.

As discussed in Section 3.7.3 the experimentally measured SCLS comprises both initial and final state effects, whereas theoretically initial as well as total SCLSs can be calculated. For a comparison between experiment and theory the total shifts (containing initial and final state contributions) are more suitable. In a previous study on the $(\sqrt{5} \times \sqrt{5})R27^\circ$ phase, where the SCLSs were used to identify the structure of the surface oxide [18], some deviations between the absolute experimental and theoretical values were observed. A reason for this could be the assumption, that there is a *complete screening* (cf. Section 3.7.3), i.e. that the energy of the photoelectron contains the whole screening energy. This complete screening picture, which works very well for transition metals [66], might not work as well for oxidic structures. If highly resolved experimental data would be available, an analysis of the line shape using a time dependent formulation [143] could provide further insight into this problem.

The calculated total SCLSs of the Pd-3d level are listed in Tab. 7.4 for the surface oxide, the surface oxide with one/two CO adsorbed in bridge sites and with one CO on a twofold by oxygen coordinated top site (top2f). The labeling of the palladium atoms follows the one shown in Fig. 6.3. Pd2a–Pd2e are the atoms in the second layer, i.e. the first Pd(100) substrate layer. For the clean $(\sqrt{5} \times \sqrt{5})R27^\circ$ structure the SCLS measurements show 3 peaks at 1.32 eV, 0.34 eV and -0.31 eV, which can directly be assigned to the fourfold, twofold and second layer Pd atoms, respectively (cf. Ref. [18]). The adsorption of CO leads to quite some changes in the SCLSs in the theoretical as well as in the experimental values. As can be seen in Tab. 7.4 the CO sitting in a bridge site induces a strong shift of ~ 0.6 eV in the SCLS of the two involved palladium atoms (Pd1c and Pd1d), whereas the other two palladium atoms in the topmost layer are only weakly affected (~ 0.15 eV). Adsorbing two CO molecules in bridge site even leads to a shift of ~ 1.2 eV for the Pd1c and Pd1d atoms compared to the clean surface oxide structure. For the CO molecule in top site it can be seen, that the SCLS of the corresponding Pd atom is strongly shifted by ~ 1.0 eV, whereas the SCLSs of the remaining Pd atoms are almost unchanged. As exemplified for the $(\sqrt{5} \times \sqrt{5})R27^\circ + \text{CO}^{\text{br}}$ structure, the SCLSs of the second layer Pd atoms are nearly not affected by the adsorption of CO. This could already be concluded by comparing the SCLSs in the initial state approximation, so that only for the $(\sqrt{5} \times \sqrt{5})R27^\circ + \text{CO}^{\text{br}}$ structure the more involved final states calculations have been performed.

Pd-atom	$\sqrt{5}$	$\sqrt{5}+\text{CO}^{\text{br}}$	$\sqrt{5}+2\text{CO}^{\text{br}}$	$\sqrt{5}+\text{CO}^{\text{top2f}}$
Pd1a(4f)	1.05	1.21	1.22	1.10
Pd1b(4f)	1.09	1.22	1.31	1.18
Pd1c(2f)	0.35	0.92	1.56	1.29
Pd1d(2f)	0.32	0.92	1.58	0.28
Pd2a	-0.24	-0.26	—	—
Pd2b	-0.25	-0.21	—	—
Pd2c	0.18	0.16	—	—
Pd2d	-0.02	0.02	—	—
Pd2e	-0.28	-0.25	—	—

Table 7.4: Calculated total SCLSs of the Pd-3d level of the $(\sqrt{5} \times \sqrt{5})R27^\circ$ surface oxide (here abbreviated with $\sqrt{5}$) and the surface oxide with one and two CO adsorbed in bridge site and one CO in a twofold by oxygen coordinated top site (top2f). The labeling of the Pd atoms follows the one in Fig. 6.3, Pd2a–Pd2e are the atoms in the first Pd(100) substrate layer. All values are in eV.

Experimentally, five peaks are found for the surface oxide structure with adsorbed CO, at 1.50 eV, 1.32 eV, 0.97 eV, 0.37 eV and -0.26 eV [142]. Again the negative shift can be assigned to the second layer Pd atoms. Comparing the remaining values to the calculated ones shows, that the Pd-3d SCLSs are not very conclusive, especially since in the experiments the coverage of CO and the ordering of the CO adlayer could not be determined. Thus, there could even be a mixture of signals coming from parts of the surface covered by the *clean* surface oxide and from parts covered by the surface oxide with one or two CO molecules in bridge sites. But also the adsorption of CO in the twofold top site can neither be confirmed, nor excluded based on these data.

Much more information about the adsorption site can be obtained by comparing the C-1s level of the adsorbed CO molecules. Since the theoretically determined absolute values of the core-level position is not very accurate, a proper reference state has to be found. Here, the C-1s level of the CO adsorbed in the $(2\sqrt{2} \times \sqrt{2})R45^\circ$ structure on Pd(100) is taken as zero reference. The calculated shifts are given in Tab. 7.5. The SCLS measurements of the C-1s level for the $(2\sqrt{2} \times \sqrt{2})R45^\circ$ and the $(\sqrt{5} \times \sqrt{5})R27^\circ$ structures with adsorbed CO are shown in Fig. 7.4. It can be seen, that the C-1s level shifts about 0.2 eV between CO adsorbed in the $(2\sqrt{2} \times \sqrt{2})R45^\circ$ and the one on the $(\sqrt{5} \times \sqrt{5})R27^\circ$. Comparing this to the theoretical results a clear distinction between the top and the bridge site can be made. For the two structures with CO in bridge sites likewise a shift of ~ 0.2 eV compared to the $(2\sqrt{2} \times \sqrt{2})R45^\circ$ is found, whereas for the CO in top site a shift of ~ 0.9 eV is calculated. The calculated C-1s SCLSs of the surface oxide structure with one and two CO in bridge sites, leading to an effective coverage of $\Theta_{\text{CO,br}} = 0.2$ ML and $\Theta_{\text{CO,br}} = 0.4$ ML with respect to the underlying Pd(100) substrate, differ only slightly. Thus, the C-1s SCLSs appear to be rather independent of the CO coverage within this range, so that it is not possible to extract information from the calculated shifts about the CO coverage during the

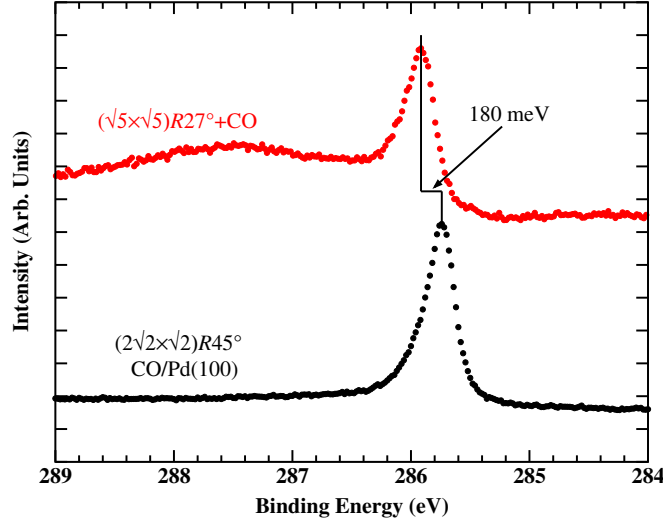


Figure 7.4: Measured C-1s surface core-level shifts of the $(2\sqrt{2} \times \sqrt{2})R45^\circ$ -CO/Pd(100) structure (black spectrum) and the $(\sqrt{5} \times \sqrt{5})R27^\circ$ +CO structure (red spectrum). In the two structures the C-1s core-level is shifted by 180 meV [142].

C-atom	$\sqrt{5}$ +CO ^{br}	$\sqrt{5}$ +2CO ^{br}	$\sqrt{5}$ +CO ^{top2f}
C-brI	—	0.19	—
C-brII	0.18	0.21	—
C-top2f	—	—	0.89

Table 7.5: Calculated total SCLSs of the C-1s level of the $(\sqrt{5} \times \sqrt{5})R27^\circ$ surface oxide (here abbreviated with $\sqrt{5}$) with one and two CO adsorbed in bridge site and one CO in a twofold top site. The labeling of the adsorption sites follows the one in Fig. 7.3. The shifts are given with respect to the C-1s level of CO adsorbed in the $(2\sqrt{2} \times \sqrt{2})R45^\circ$ structure on Pd(100). All values are in eV.

experiments. Hence, it remains unclear, how much CO was adsorbed on the surface during the SCLS measurements.

Even though the calculated SCLSs include some uncertainties regarding the computational setup and the artificial interaction between the charged, periodic images due to the supercell approach (cf. Section 3.7.3), these results are rather definite with respect to the adsorption site. Thus, experimentally as well a theoretically the bridge site appears to be the most favorable for the adsorption of CO on the $(\sqrt{5} \times \sqrt{5})R27^\circ$ surface oxide structure.

7.3 Phase Diagram For Pd(100) In An O₂ And CO Gas Phase

Within the atomistic thermodynamics approach it is now possible to directly compare the stability of all proposed structures in equilibrium with an oxygen and CO gas phase. In the here discussed case of a two-component gas phase a *constrained* equilibrium is considered, i.e. the surface is in equilibrium with both the oxygen and the CO gas phase, but the two gas phases are not in thermodynamic equilibrium with each other (cf. Page 39). Thus, the formation of CO₂ is neglected in the gas phase, as well as on the surface. In the gas phase this assumption seems to be reasonable, since in reality the reaction of O₂ and CO is kinetically hindered due to a huge reaction barrier. At the surface, though, where the reaction is actually supposed to take place, this is only appropriate as long as the on-going catalytic formation of CO₂ is less frequent than all O₂ and CO adsorption and desorption processes, so that the surface can still maintain its equilibrium with the two gas phase components. Thus, the constrained atomistic thermodynamics approach can be used here only to obtain a first idea of relevant surface phases in the whole (T, p) -range of gas phase conditions. These results can then provide the basis for the next refining step, the consideration of the reaction kinetics on the average surface composition by kinetic Monte Carlo simulations, which will be discussed in the next Chapter.

To calculate the Gibbs free energy of adsorption depending on both the O₂ and CO gas phase conditions Eq. (4.31) is used

$$\begin{aligned}
 \Delta G^{\text{ads}}(\Delta\mu_{\text{O}}, \Delta\mu_{\text{CO}}) &= \\
 &= -\frac{1}{A} \left(E_{\text{O,CO@Pd}}^{\text{surf}} - E_{\text{Pd}}^{\text{surf}} - \Delta N_{\text{Pd}} E_{\text{Pd}}^{\text{bulk}} - N_{\text{O}}(1/2 E_{\text{O}_2}^{\text{tot}} + \Delta\mu_{\text{O}}) - N_{\text{CO}}(E_{\text{CO}}^{\text{tot}} + \Delta\mu_{\text{CO}}) \right) \\
 &= -\frac{1}{A} \Delta \tilde{E}_{\text{O,CO@Pd}}^{\text{bind}} + \frac{N_{\text{O}}}{A} \Delta\mu_{\text{O}} + \frac{N_{\text{CO}}}{A} \Delta\mu_{\text{CO}} \quad .
 \end{aligned} \tag{7.3}$$

Just as in the previous Section the Gibbs free energies of the different subsystem are approximated by the DFT total energies (for a detailed discussion of the computational setup cf. Appendix A). As discussed in Section 6.2, for the here investigated systems the pV -term as well as the configurational entropy term stay below 3 meV/Å², which does not decisively influence the results. The magnitude of the vibrational contribution, on the other hand, has to be estimated for every considered structure. For oxygen containing structures this has already been done in Section 6.2. New vibrational contributions arise from CO containing structures. Here, the vibrational contribution comprises two different components, the change in the C-O vibration due to the adsorption and an additional Pd-C vibration. For the $(2\sqrt{2} \times \sqrt{2})R45^\circ$ -CO/Pd(100) structure this is given by (cf. Section 6.2)

$$\Delta G^{\text{ads,vib}}(T) = -\frac{2}{A} \left(F^{\text{vib}}(T, \bar{\omega}_{\text{C-Pd}}^{\text{surf}}) + F^{\text{vib}}(T, \bar{\omega}_{\text{O-C@Pd}}^{\text{surf}}) - F^{\text{vib,ZPVE}}(\bar{\omega}_{\text{CO}}^{\text{gas}}) \right) \quad . \tag{7.4}$$

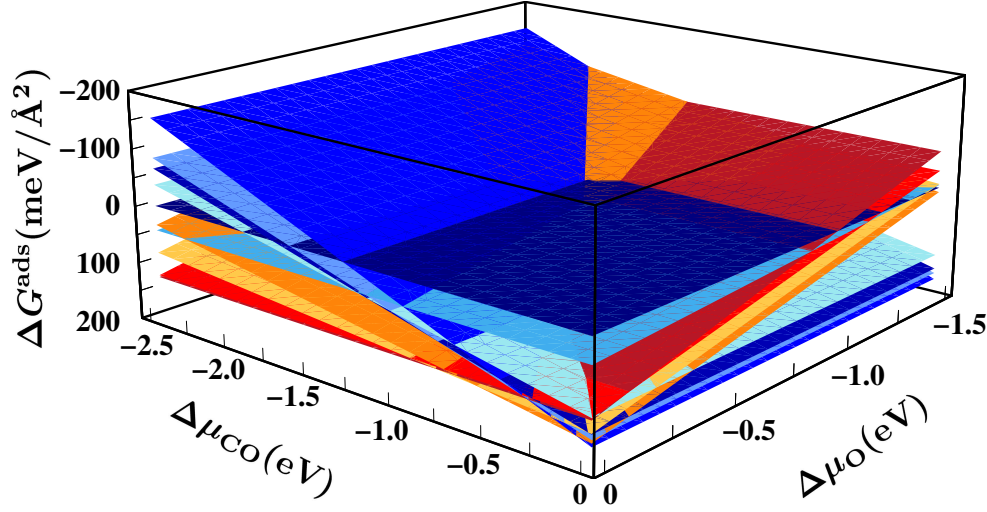


Figure 7.5: Gibbs free energy of adsorption for the Pd(100) surface in a constrained equilibrium with an O₂ and CO gas phase. The different planes represent the 9 most stable structures. Depending on their O and CO coverage the different planes have a slope with respect to $\Delta\mu_{\text{O}}$ and/or $\Delta\mu_{\text{CO}}$

Assuming average frequencies of $\bar{\omega}_{\text{C-Pd}}^{\text{surf}} = 41 \text{ meV}$ [129], $\bar{\omega}_{\text{O-C@Pd}}^{\text{surf}} = 242 \text{ meV}$ [127] and $\bar{\omega}_{\text{CO}}^{\text{gas}} = 269 \text{ meV}$ [11], the vibrational contribution to the Gibbs free energy of adsorption for this structure stays below $2 \text{ meV}/\text{\AA}^2$ for temperatures up to $T = 600 \text{ K}$. Since this contribution is proportional to the coverage, even for a (1×1) structure it will only increase up to $4 \text{ meV}/\text{\AA}^2$, which is still rather small. Regarding mixed structures containing oxygen and CO the different contributions will simply add up, e.g. for a (2×2) unit cell with one O in hollow and one CO in bridge site the vibrational contribution is less than $1.6 + 0.8 = 2.4 \text{ meV}/\text{\AA}^2$ in the investigated temperature range (cf. Page 71). Similarly this is done for the co-adsorbed structures on the surface oxide. The additional adsorption of one CO molecule in the $(\sqrt{5} \times \sqrt{5})R27^\circ$ surface unit cell results in an increase of less than $1 \text{ meV}/\text{\AA}^2$ in the vibrational contribution, so that for these structures the estimate given in Section 6.2 is almost unchanged. The phase diagram discussed in the following is not significantly changed, if these estimated, maximum values for the vibrational contribution are included, i.e. there are some small shifts in the boundaries between stable phases, but none of the stable structures disappears from and none of the unstable ones appears in the phase diagram.

In Fig. 7.5 the Gibbs free energy of adsorption is shown as a function of the chemical potentials of oxygen and CO. Every plane in this graph belongs to a specific structure and its slope in x - and y -direction depends on the oxygen and CO coverage, respectively. In this study the thermodynamic stability of a total number of 189 structures is compared, comprising of all the afore described possibilities to adsorb O and/or CO on Pd(100) including the (modified) $(\sqrt{5} \times \sqrt{5})R27^\circ$ surface oxide structures. Only

the planes belonging to the 11 most stable phases are shown in Fig. 7.5. The most stable phase is again the one that maximizes ΔG^{ads} for any given chemical potential $\Delta\mu_{\text{O}}$ and $\Delta\mu_{\text{CO}}$, i.e., since the z -axis is inverted in Fig. 7.5, this is the structure with the *lowest* plane (cf. Section 4.3). Two structures having the same number of oxygen and CO atoms/molecules per surface area will result in parallel planes, so that the one with the smaller binding energy $\tilde{E}_{\text{O,CO@Pd}}^{\text{bind}}$ can directly be excluded as a stable structure (cf. Appendix B.1).

In this 3-dimensional plot, the dependence of ΔG^{ads} on the chemical potentials is nicely visualized, but the most stable phase at a specific value of $\Delta\mu_{\text{O}}$ and $\Delta\mu_{\text{CO}}$ is rather difficult to identify. For this the 3D-plot can be converted into a 2D-plot by looking from below at the graph in Fig. 7.5. The resulting 2D-surface phase diagram is shown in Fig. 7.6. Here, only the most stable phases at any given chemical potential of oxygen and CO are displayed. For a more intuitive understanding the chemical potentials have been converted into the respective pressure scales at $T = 300$ K and 600 K in the top two x -axes for oxygen and in the right two y -axes for CO. Starting at the lower left corner of Fig. 7.6, which corresponds to both very O-poor and CO-poor gas phase conditions, the clean metal surface must obviously result as the most stable system state. Moving from this situation to the right, i.e. keeping the CO chemical potential at this very low value and increasing the oxygen chemical potential leads to the same result as discussed for the pure O_2 gas phase in Section 6.2. First, the $p(2 \times 2)$ adlayer becomes stable, then the $(\sqrt{5} \times \sqrt{5})R27^\circ$ surface oxide and finally the bulk oxide.

If instead the oxygen content is kept low and the CO content is gradually increased in the gas phase, i.e. moving from the lower left corner upwards, a series of ordered CO adlayer phases on Pd(100) with increasing coverage is stabilized. At first the also experimentally observed $(2\sqrt{2} \times \sqrt{2})R45^\circ$ (0.5 ML), $(3\sqrt{2} \times \sqrt{2})R45^\circ$ (0.67 ML) and $(4\sqrt{2} \times \sqrt{2})R45^\circ$ (0.75 ML) structures are found and finally for a very high CO content in the gas phase a (1×1) structure with CO in bridge site (1.0 ML) is stable.

Starting again in the lower left corner and moving along the diagonal, i.e. increasing now both the oxygen as well as the CO content in the gas phase, one would intuitively expect a mixture of the so far discussed phases, i.e. co-adsorbed structures of oxygen and CO, to become favorable. As can be seen in Fig. 7.6 none of the above presented structural models for ordered overlayers of O and CO on Pd(100) (cf. Fig. 7.2) is a thermodynamically most stable phase under any gas phase conditions. This is in agreement with the already above mentioned experimental findings, that on Pd(100) O and CO prefer to form separate domains rather than any ordered co-adsorbed overlayers [110]. The low stability of these ordered co-adsorbed phases can thus be explained by the strongly repulsive interactions between the two adsorbates leading to a significant decrease in the binding energies. Nevertheless, it can not be excluded that ordered arrangements with another periodicity would not lead to a lowering in the repulsive interactions. To take a reasonable part in the phase diagram, though, the binding energies would have to increase by as much as 0.3–0.5 eV per O atom/CO

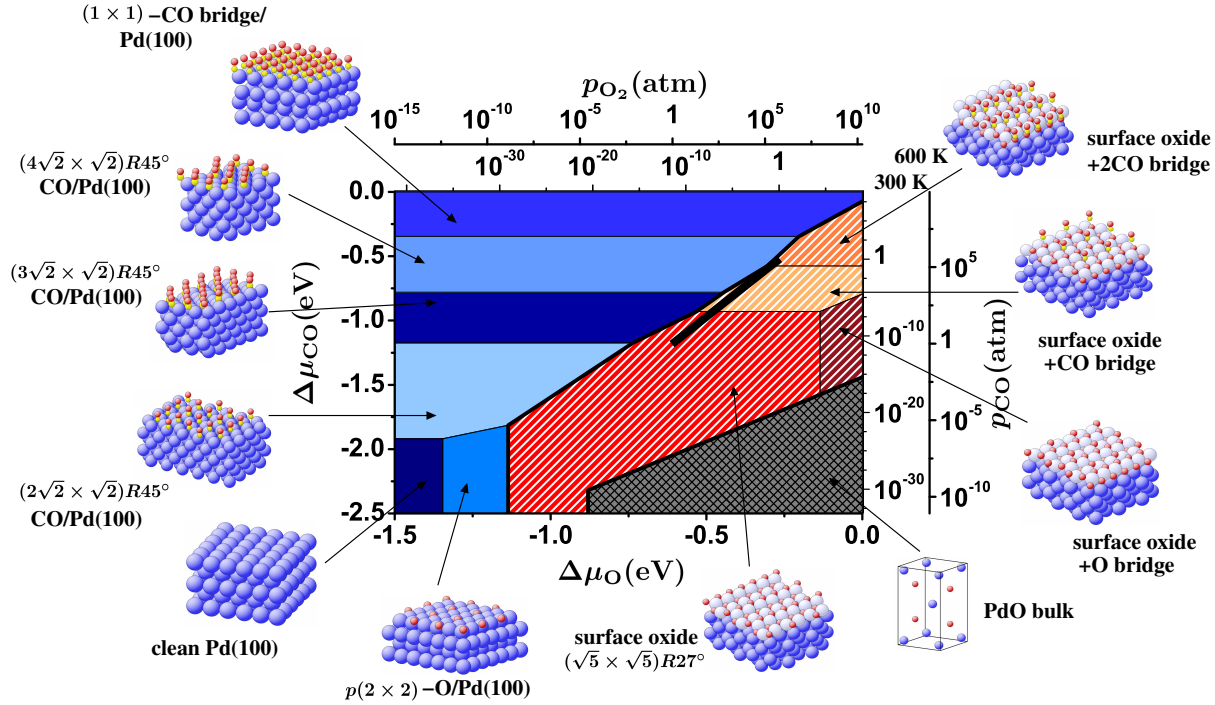


Figure 7.6: Surface phase diagram for the Pd(100) surface in a constrained equilibrium with an O_2 and CO gas phase. The atomic structures underlying the various stable (co-)adsorption phases on the metal and the surface oxide as well as a thick bulk-like oxide film (indicated by the bulk unit cell) are also shown (Pd = large blue spheres, O = small red spheres and C = small yellow spheres). The black bar marks gas phase conditions representative of technological CO oxidation catalysis, i.e. partial pressures of 1 atm and temperatures between 300–600 K.

molecule compared to the now proposed structures. Compared to the pure overlayer structures this would even imply attractive interactions between the two species.

Instead of co-adsorbed structures on Pd(100), for high oxygen and high CO content in the gas phase (upper right part in Fig. 7.6) co-adsorbed structures involving the $(\sqrt{5} \times \sqrt{5})R27^\circ$ surface oxide become stable (two orange-white hatched regions). These two structures correspond to the surface oxide with one and two additional CO adsorbed in bridge sites, respectively (cf. Fig. 7.3 and structures 1 and 15 in Appendix B.1). Additional oxygen adsorption in the bridge site of the surface oxide leads also to a stable phase in a small range of very oxygen-rich and intermediate CO conditions (dark red-white hatched region, structure 99). It is remarkable, that the bulk oxide is already decomposed to CO_2 and the pure Pd metal under these conditions, whereas the surface oxide is still stable. The stability region of the bulk oxide has been determined via Eq. (4.35), yielding for the specific case of PdO

$$\Delta\mu_{\text{CO}} - \Delta\mu_{\text{O}} < -2\Delta G_{\text{PdO}}^f(0,0) + \Delta E^{\text{mol}} \quad . \quad (7.5)$$

The calculated as well as the experimental values of the binding energies of the three

	PBE	RPBE	LDA	Exp. [11]
O ₂	-6.20	-5.75	-7.56	-5.17
CO	-11.65	-11.20	-12.93	-11.16
CO ₂	-17.99	-17.09	-20.43	-16.68
ΔE^{mol}	-3.24	-3.02	-3.72	-2.93

Table 7.6: Theoretical and experimental binding energies of O₂, CO and CO₂. All values are in eV.

involved gas phase species needed to evaluate ΔE^{mol} are listed in Tab. 7.6. A detailed discussion of the accuracy of the molecular binding energies is given in Appendix A.3. The heat of formation $\Delta G_{\text{PdO}}^f(0,0)$ is given in Tab. 6.4.

All other investigated adlayer structures on Pd(100) or structures involving the $(\sqrt{5} \times \sqrt{5})R27^\circ$ surface oxide (listed in Appendix B.1) do not appear as stable phase in the shown range of O and CO chemical potentials.

Looking again at the whole phase diagram 11 different phases can therefore be identified, divided into three groups. All phases involving adlayer structures on the Pd(100) surface are colored in blue, all phases involving the $(\sqrt{5} \times \sqrt{5})R27^\circ$ surface oxide are red/orange-white hatched and the bulk oxide is grey cross-hatched. In addition, gas phase conditions representative of technological CO oxidation catalysis, i.e. partial pressures of 1 atm and temperatures between 300–600 K, are marked by a black bar. Focusing only on these three different groups of phases two important conclusions with respect to the relevance of the surface oxide under reaction conditions can be drawn. First, the formation of bulk oxide (grey cross-hatched) at the surface under ambient gas phase conditions of O₂ and CO (black bar) can be ruled out. And second, the stability region of the surface oxide does, however, extend to such conditions. In fact, it is either this monolayer thin surface oxide or the CO adlayers on Pd(100) as neighboring phases around the catalytically active region in (T, p) -space.

As already done for the phase diagram in a pure oxygen gas phase in Section 6.2 the dependence of the obtained results on the employed exchange-correlation functional is checked by reevaluating the phase diagram using the RPBE and LDA. For this only the 11 different phases identified using the PBE functional above are recalculated. The Gibbs free energies of adsorption are listed in Tab 7.7 and the two respective phase diagrams are shown in Fig. 7.7. The phase diagram obtained within the RPBE approximation (left graph in Fig. 7.7) looks in fact very similar to the previously discussed one. There are some shifts in the phase boundaries and the high coverage phases of oxygen and CO, $(\sqrt{5} \times \sqrt{5})R27^\circ + \text{O}^{\text{br}}$ and $(1 \times 1)\text{-CO}^{\text{br}}/\text{Pd}(100)$, are not stable anymore in the shown range of chemical potentials, but again the catalytically active region (black bar) is directly at the phase boundary between surface oxide structures and CO adlayers on Pd(100). Due to the smaller heat of formation (cf. Tab. 6.4) the stability region of the bulk oxide is even further away from ambient conditions of oxygen and CO. Even if the LDA is used as exchange-correlation func-

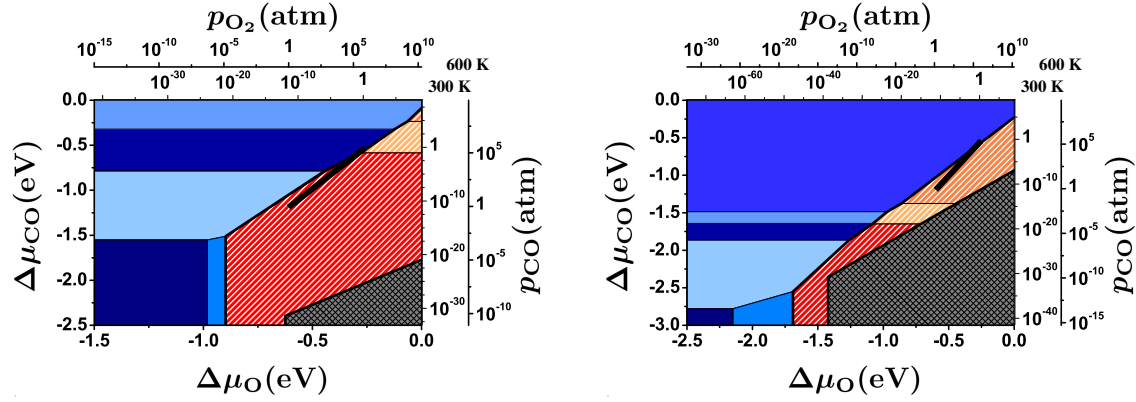


Figure 7.7: Surface phase diagram for the Pd(100) surface in a constrained equilibrium with an O_2 and CO gas phase. The left plot shows the RPBE results and the right one the LDA results. The color coding of the different phases is equivalent to the one used in Fig. 7.6. The black bar marks again gas phase conditions representative of technological CO oxidation catalysis, i.e. partial pressures of 1 atm and temperatures between 300–600 K.

	Θ_O	Θ_{CO}	$\Delta G^{ads}(0,0)$		
			PBE	RPBE	LDA
clean Pd(100)	0.00	0.00	0	0	0
$p(2 \times 2)\text{-O/Pd(100)}$	0.25	0.00	-43	-31	-73
$(\sqrt{5} \times \sqrt{5})R27^\circ$	0.80	0.00	-123	-93	-199
$(\sqrt{5} \times \sqrt{5})R27^\circ + O^{br}$	1.00	0.00	-127	-90	-219
$(2\sqrt{2} \times \sqrt{2})R45^\circ\text{-CO/Pd(100)}$	0.00	0.50	-123	-98	-186
$(3\sqrt{2} \times \sqrt{2})R45^\circ\text{-CO/Pd(100)}$	0.00	0.67	-148	-114	-231
$(4\sqrt{2} \times \sqrt{2})R45^\circ\text{-CO/Pd(100)}$	0.00	0.75	-157	-117	-250
$(1 \times 1)\text{-CO}^{br}/\text{Pd(100)}$	0.00	1.00	-168	-113	-300
$(\sqrt{5} \times \sqrt{5})R27^\circ + CO^{br}$	0.80	0.20	-147	-108	-244
$(\sqrt{5} \times \sqrt{5})R27^\circ + 2CO^{br}$	0.80	0.40	-162	-114	-282

Table 7.7: Gibbs free energy of adsorption for all relevant structures of the Pd(100) surface in a constrained thermodynamic equilibrium with an O_2 and CO gas phase. The coverage is given with respect to a Pd(100)-(1 \times 1) surface unit cell. All values are in meV/ \AA^2 .

tional (right plot in Fig. 7.7), which shows a strong over-binding in the here discussed systems, the stability region of the bulk oxide does not extend to the catalytically relevant gas phase conditions, although it covers a much larger range compared to the phase diagrams obtained within the two GGA functionals. It should also be noted, that in the LDA phase diagram the range of O and CO chemical potentials is enlarged to somewhat lower values to include the stability region of the clean metal surface.

7.4 Conclusions

The stability of the Pd(100) surface has been investigated in a constrained equilibrium with an O₂ and CO gas phase. To setup the surface phase diagram a large number of different structures having O and CO adsorbed in high symmetry sites on the Pd(100) surface and on the $(\sqrt{5} \times \sqrt{5})R27^\circ$ surface oxide structure have been included. It is found that under gas phase conditions of ambient temperatures and pressures, as applied in heterogenous oxidation catalysis, it is either the nanometer thin surface oxide structure or a CO covered Pd(100) surface that is stable, whereas the stability region of the bulk oxide does not extend to these conditions.

To obtain an estimate of the uncertainty introduced by the choice of a specific exchange-correlation functional the calculations are performed using the PBE, RPBE and LDA. Comparing the phase diagrams for these three different exchange-correlation functionals shifts in the positions of the boundaries between the different stable phases can be observed. But it can also be seen that the position of the boundary between the CO covered Pd(100) phases and the $(\sqrt{5} \times \sqrt{5})R27^\circ$ surface oxide structures does in fact agree very well. In all three cases, the catalytically active region is very close to this boundary, but still within the stability range of the surface oxide, whereas the formation bulk oxide appears to be unfavorable. Thus, these conclusions seem to be independent of the chosen exchange-correlation functional.

Since in this approach a constrained equilibrium is assumed, the stability of the surface oxide could still be reduced by the reaction kinetics, if the catalytic CO₂ formation consumes the surface oxygen species faster than they can be replenished from the gas phase. The onset of the surface oxide decomposition including the on-going catalytic reaction will be discussed in the next Chapter.

